Downscaling Sentinel-3 Chlorophyll-a Concentration for Inland Lakes Based on Multivariate Analysis and Gradient Boosting Decision Trees Regression

Simin Zhang, Nanfeng Liu, Ming Luo, Tao Jiang, Ting On Chan, Cynthia Sin Ting Yau, and Yeran Sun

***Abstract*—Downscaling Chlorophyll-a (Chl-a) concentration derived from satellite image is crucial for refined applications such as water quality monitoring. However, the precision of downscaling is usually constrained by various environmental factors. In this paper, we develop a downscaling method for Chl-a concentration to improve precision, especially for inland lakes with different surrounding environment. The method downscales the Sentinel-3 Chl-a concentration from 300 m to 30 m, based on the multivariate analysis (MVA) and the gradient boosting decision tree (GBDT) model. Firstly, we analyzed 21 Chl-a concentration related indices to identify optimal factors for Chl-a concentration variability. Secondly, a GBDT model is constructed to convey the non-linear relationship between the optimal factors and Chl-a concentration at coarse resolution. Finally, fine-resolution Chl-a concentrations were produced by employing the model to refine cofactors for 12 distinct lakes. The results indicated that the proposed MVA-GBDT method effectively inferred the variability of Chl-a concentration with a mean RMSE of 4.505 mg/m^3, an improvement of 5%–39% over other methods. Furthermore, for lakes with large water quality heterogeneity, the method led to a cross validation RMSE and a difference in accuracy of 5.371 mg/m^3 and 0.866 mg/m^3, respectively. In addition, this study examined the significance of the auxiliary factors and found that the NDCI and WST were the two most important factors for MVA-GBDT to detect Chl-a concentration distributions, particularly for NDCI in lakes with high nutrient contrasts. These findings contribute to the generation of fine-scale Chl-a concentrations in lakes and support related applications.**

Manuscript received 20 April 2023; revised 26 June 2023; accepted 26 July 2023. Date of publication 3 August 2023; date of current version 7 September 2023. This work was supported by the National Key R&D Program of China under Grant 2019YFC1510400. *(Corresponding author: Ting On Chan.)*

Simin Zhang, Nanfeng Liu, and Tao Jiang are with the School of Geography and Planning, Sun Yat-sen University, Guangzhou 510275, China (e-mail: zhangsm39@mail2.sysu.edu.cn; liunf3@mail.sysu.edu.cn; eesjt@mail.sysu.edu.cn).

Ming Luo is with the Guangdong Provincial Key Laboratory of Urbanization and Geo-Simulation, Sun Yat-sen University, Guangzhou 510275, China (e-mail: luom38@mail.sysu.edu.cn).

Ting On Chan is with the Guangdong Provincial Engineering Research Centre for Public Security and Disasters, Sun Yat-sen University, Guangzhou 510275, China, and also with the Guangdong Provincial Key Laboratory of Urbanization and Geo-Simulation, Sun Yat-sen University, Guangzhou 510275, China (e-mail: chantingon@mail.sysu.edu.cn).

Cynthia Sin Ting Yau is with the Department of Ocean Science, Hong Kong University of Science and Technology, Hong Kong, SAR, China (e-mail: cynthiastyau@ust.hk).

Yeran Sun is with the Department of Geography, College of Science, University of Lincoln, LN6 7TS Lincoln, U.K. (e-mail: yesun@lincoln.ac.uk).

Digital Object Identifier 10.1109/JSTARS.2023.3301791

***Index Terms*—Chlorophyll-a (Chl-a) concentration, downscaling, gradient boosting decision tree (GBDT), lake ecosystems.**

I. Introduction

LAKES are often the main local source of drinking water. Besides, the lakes not only contribute directly to the existence and development of human activities (e.g., fish farming) but also have a significant impact on worldwide biochemical cycles and local ecosystems [1], [2], [3]. Nevertheless, the lakes are becoming increasingly eutrophic, as their water quality is deteriorating due to climate change and human activities. For instance, a research item assessing the trophic conditions of lakes ($>$10 km^2) globally showed that in the summer of 2012, 63% of lakes were eutrophic, 26% were mesotrophic, and 11% were hypertrophic [4].

Chlorophyll-a (Chl-a), is a photosynthesis compound existing in every algal plant. Its concentration reflects the biomass of phytoplankton, which is closely linked to nutrient concentrations and is a representative metric for assessing the extent of hypotrophy and water quality in lakes [5], [6]. However, Chl-a concentration measurements often require field sampling and in-laboratory work, which is time-consuming and relatively costly. Furthermore, given the rapid growth rate of phytoplankton, the high variability of the inland conditions suppresses the availability of reliable Chl-a concentration [7].

Remote sensing techniques have evolved rapidly during the last few decades. They appear to be a viable and sometimes the only solution to make measurements over a large area, as they have the prospect of providing contiguous data with high spatial coverages [8]. The Chl-a concentration can be assessed by using reflectance measurements from sensors mounted on satellites. Several sensors on board the satellites collect Chl-a concentration information in water columns at different spatial and temporal resolutions. These sensors include MODIS-Aqua [9], VIIRS sensor on the NOAA-20 meteorological satellite [10], OLI sensor on Landsat 8 [11], and MSI on Sentinel-2 satellites [12]. MODIS-Aqua is generally considered to be effective in providing raw information for global Chl-a concentrations [13]. While the MODIS-Aqua's temporal resolution (1 day) renders its measurements ideal for continual monitoring, the 1-km resolution is too coarse for inland lake monitoring.

The Sentinel-3 OLCI sensor is the new generation that is currently regarded as the most compatible sensor for remote

sensing of the watercolor of lakes [14], [15], [16] since its launch in 2016. The Sentinel-3 OLCI provides two types of Chl-a concentrations: the open ocean and complex water Chl-a concentrations. The complex water Chl-a concentration is engineered for complicated waters by applying the neural network (NN) method [17]. While this provides a feasible solution for assessing Chl-a concentration of the lake surface with different water nutrient content, the quality of data decreases at local levels, especially for spatially complicated small and medium-sized inland lakes.

A possible solution to improve the coarse spatial resolution of Chl-a concentration is to develop spatial downscaling algorithms that use high-resolution satellite reflectance [10]. Spatial downscaling techniques have been used for numerous satellite images, such as land surface temperatures [18], [19], [20], [21], precipitations [22], [23], [24], [25], and soil moistures [26], [27], [28], [29]. For Chl-a concentration, Fu et al. [30] first represented coastal Chl-a concentration as a polynomial function of the Landsat OLI optimal band and its combination, based on the assumption that the scale is invariant. Since then, several modified versions of the method have been proposed, using different regression methods, or incorporating various auxiliary factors. In particular, machine learning (ML) approaches have been incorporated into different methods for downscaling. For example, the random forest (RF), the support vector regression, and the genetic programming method [31], [32], are used for the downscaling. Although the ML methods have shown promising results in Chl-a concentration downscaling, their application is limited to large coastal areas due to the coarse resolution of MODIS. For inland lakes, which are relatively small in area and subject to natural and anthropogenic influences, there has been little exploration in the literature. Therefore, we develop a method for downscaling Sentinel-3 Chl-a concentration to a fine resolution of 30 m to support related applications in various lakes across China.

There are two main components of the proposed method: the determination of the downscaling algorithm and the selection of auxiliary factors. As for downscaling algorithm, because Chl-a concentration and surface features have a complex nonlinear relationship, the ML techniques often perform better than traditional statistical regression algorithms for downscaling [32]. The gradient boosting decision tree (GBDT) is a ML algorithm that integrated different decision trees to produce a reliable method [33], but its application in downscaling has rarely been explored. Besides, the Chl-a concentration spatial distribution of lakes varies greatly due to China's complex topographic and climatic characteristics. As a result, the training data for ML modeling may be biased. The GBDT is an iterative approach resistant to exceptions and inconsistent values, resulting in consistent performance. Thus, adapting GBDT to downscale satellite-derived Chl-a concentration becomes the motivation behind this work.

The auxiliary factors mostly used for Chl-a concentration extraction are spectral reflectance and their derivatives. For example, they are texture and thermal features [34], [35], [36]. Recently, some factors derived from vegetation red-edge bands have been shown to be strongly related to the Chl-a concentration [37], [38]. However, most dated sensors lacked red-edge bands, making these factors difficult to be considered in the models. Fortunately, the Sentinel-2 satellites established three bands in the vegetation red-edge region (670–760 nm), providing effective datasets complement to phytoplankton monitoring for lakes.

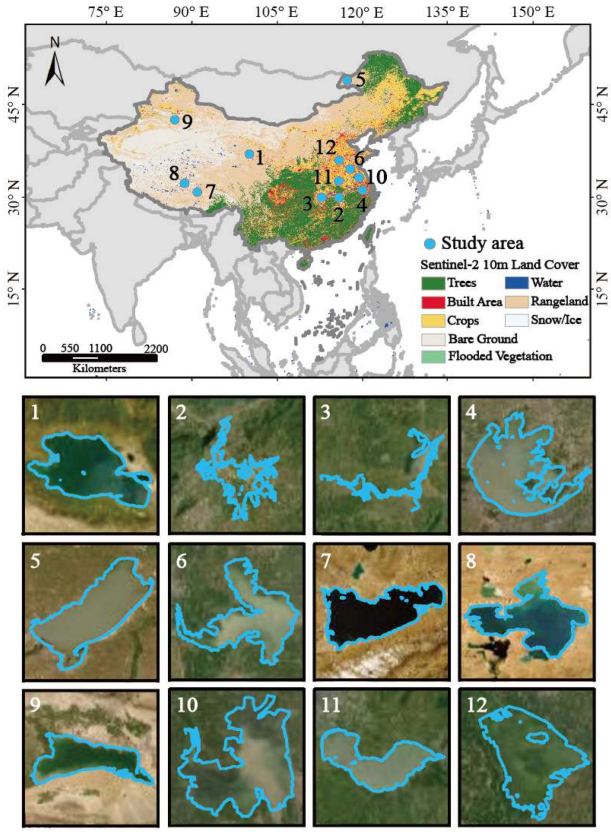

Fig. 1. Twelve lakes (Lakes 1–12) in China are represented spatially along with the corresponding Sentinel-2 true color images.

This article presented a method downscaling Sentinel-3 Chl-a concentration by adapting multivariate analysis (MVA) and GBDT algorithm, leading to a more refined application in lake surface monitoring. To extract as much information related to Chl-a concentration from satellite observations as possible, the optical bands of Sentinel-2 and its derived red-edge indices, chlorophyll indices, and texture features (TF), the backscattering characteristics of Sentinel-1, and the thermal features of Landsat-8 were treated as the auxiliary factors to synthetically characterize the targeted lake's ecological or geographic features.

II. Study Area and Experimental Data

A. Study Area

Twelve inland lakes (Lakes 1–12, area $>1000\ \text{km}^2$, including the top five lakes) distributed across China were selected as study areas (see Fig. 1). As can be seen, owing to a large distribution, the selected lake ecosystems vary considerably in terms of land cover type (trees, bare ground, snow, etc.), lake water quality status (oligotrophic, mesotrophic, and eutrophic), climate zone (warm temperate, subtropical, mid-temperate, and

plateau climatic), and lake type (brackish and freshwater lakes); more details about the selected lakes can be found in Table IV (see Appendix).

B. Chl-a Concentration Products

We obtained images of each lake for different months in 2021 from the Sentinel-3 OLCI dataset provided by the European Space Agency (https://sentinel.esa.int/web/) (see Table IV for details). Their surface reflectance from the image dataset in the Sentinel-3 optical bands was first processed with radiometric calibration and atmospheric correction. Then, an integrated Case 2 Regional Coast Color (C2RCC) algorithm based on NN technology, embedded in the Sentinel toolbox in the Sentinel Application Platform, was used to invert Sentinel-3 Chl-a concentration images [39]. After that, the water body was extracted from each processed image to obtain the Chl-a concentration map.

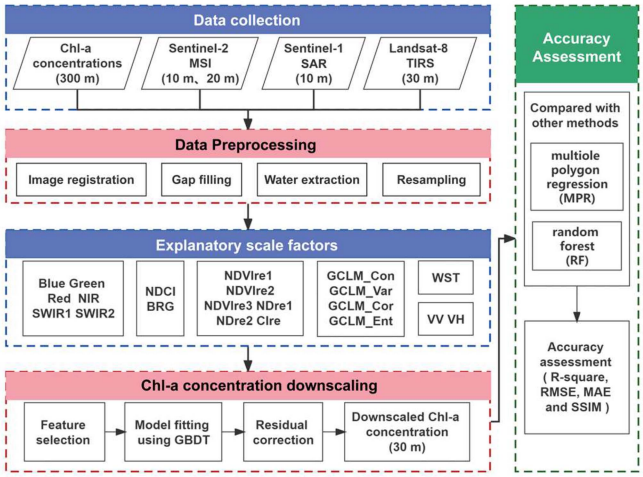

Fig. 2. Workflow of the proposed method.

C. Auxiliary Datasets Acquisition

In this study, we acquired fine-resolution auxiliary data from three major satellite datasets: Sentinel-1, Sentinel-2, and Landsat-8. We downloaded the Sentinel-1 synthetic aperture radar (SAR) and the Sentinel-2 multispectral instrument (MSI) data from the Copernicus Open Access Hub (https://scihub.copernicus.eu/) and the Landsat-8 level-2 data from the United States Geological Survey site (https://earthexplorer.usgs.gov/). The products covered a timeframe of January 1 to December 31, 2019, with revisit frequencies of 12 days for Sentinel-1, 5 days for Sentinel-2, and 16 days for Landsat-8. Due to cloud cover and the quality of remote-sensing reflectance, only a few matched dates with valid data that met the criteria of cloud coverage $< 10\%$ over the study region, were chosen for input in the downscaling model. Finally, we obtained available satellite images of each lake for matching acquisition dates during 2019. Detailed temporal information is shown in Table IV (see Appendix).

III. Methodology

The proposed method integrated the MVA and the GBDT regression, avoiding the GBDT being overfitted even under more than 20 types of features used as input for training, resulting in an accurate downscaling of the Sentinel-3 Chl-a concentration from 300 to 30 m for inland lakes with a large discrepancy in nutrient status and surrounding environment. The proposed MVA-GBDT method consists of four steps, including a thorough accuracy assessment scheme, as shown in Fig. 2. Each step will be described in the following sections in detail.

A. Step 1: Data Preprocessing

To reduce geometric mismatches between various datasets, image registration tools from the ENVI software package were applied. Subsequently, for the Sentinel-1 and Sentinel-2 reflectance, the Savitzky–Golay filter was utilized to generate gap-filled reflectance data. For water surface temperature (WST) obtained from Landsat-8, cloud-free time series were reconstructed using the harmonic analysis of time series method. This method has been widely used to reconstruct time series of LST and NDVI to remove random noise or eliminate cloud/snow contamination. [40], [41]. Next, the modified normalized difference water index (MNDWI) was adopted to recognize water masses [42]. The MNDWI thresholds for water mass recognition were determined by iteratively computing the output. After that, the optimal thresholds were used for the high-resolution images. Finally, all the auxiliary data were resampled from 300 and 30 m for model training and prediction using the cubic convolutional interpolation resampling method [43]. This creates a correspondence between the satellite products and the Chl-a concentrations.

B. Step 2: Explanatory Factors Selection

According to the literature on Chl-a concentration analysis (e.g., [30], [31], and [32]), it is realized that the Chl-a concentration is relatively sensitive to spectral reflectance, TF, and water temperature. Furthermore, some literature (e.g., [37], [38], [44], and [45]) suggest that chlorophyll and red-edge indices are essential for the extraction of Chl-a concentration. As a result, in this work, 21 indicators (including optical bands, water temperature, normalized difference chlorophyll index (NDCI), chlorophyll index red-edge, etc.) were selected by integrating multisource satellite data to construct a comprehensive Chl-a indicator system (as shown in Table I). These indicators can be broadly classified into the following six types.

1) Multispectral reflectance, which is widely considered an important parameter for Chl-a inversion (e.g., [30], [31], and [32]), mainly consists of the visible, near-infrared (NIR), and shortwave infrared (SWIR) bands. They characterize differences in the surface reflection of solar radiation.
2) Chlorophyll indices, including the NDCI [44] and the blue-red-green index (BRG) [45], which are specifically designed for the inversion of chlorophyll in water bodies.
3) Red-edge index, which is calculated from the unique red-edge bands of Sentinel-2 imagery. The red-edge indices derived from vegetation red-edge bands have been

TABLE I
DESCRIPTION OF THE FACTOR SET FOR DOWNSCALING

Data Type	Nomenclature	Abbr.	Descriptions	Data Source	Resolution (m)
Multispectral reflectance (SR)	Blue	B	Visible light band	Sentinel-2 MSI	10
	Green	G			
	Red	R			
	Near-infrared	NIR	Near infrared light band		
	Short-wave infrared 1	SWIR 1	Short-wave infrared light band		20
	Short-wave infrared 2	SWIR 2			
Chlorophyll index (CI)	Normalized difference chlorophyll index	NDCI	(NIR−Red)/(NIR+Red)	Sentinel-2 MSI	10
	Blue-red-green index	BRG	(Blue - Red)/Green		
Red-edge index (REI)	Normalized difference vegetation index red-edge1	NDVIre1	(RE 4−RE1) / (RE 4+RE 1)	Sentinel-2 MSI	20
	Normalized difference vegetation index red-edge2	NDVIre2	(RE 4−RE 2) / (RE 4+RE 2)		
	Normalized difference Vegetation index red-edge3	NDVIre3	(RE 4−RE 3) / (RE 4+RE 3)		
	Normalized difference red-edge 1	NDre1	(RE 2−RE 1) / (RE 2+RE 1)		
	Normalized difference red-edge 2	NDre2	(RE 3−RE 1) / (RE 3+RE 1)		
	Chlorophyll index red-edge	CIre	(RE 3/RE 1)-1		
Texture feature (TF)	Correlation	GCLM_Cor	Image texture characteristics	Sentinel-2 MSI	10
	Variance	GCLM_Var			
	Contrast	GCLM_Con			
	Entropy	GCLM_Ent			
Thermal characteristic (TC)	Water surface temperature	WST	Surface condition	Landsat-8 OLI/TIRS	30
Backscattering characteristic (BC)	Vertical transmit/vertical receive	VV	Backscattering features	Sentinel-1 SAR GRD	10
	Vertical transmit/horizontal receive	VH			

shown to be strongly correlated to the Chl-a concentration [37], [38].

4) TF, which include correlation, contrast, entropy, and variance. Some researchers have suggested that texture information can enhance the precision of Chl-a concentration assessment [46], [47]. Thus, several TF obtained by using the widely used gray scale co-occurrence matrix method were selected as Chl-a concentration factors.
5) Backscattering characteristics, derived from the Sentinel-1 SAR image. The vertical transmit/vertical receive (VV) and vertical transmit/horizontal receive (VH) bands are used to capture the topographic features of inland lakes as supplementary information.
6) Thermal characteristics (TC), derived from the Landsat-8 thermal infrared sensor (TIRS) imagery. According to Quiros et al. [48], the WST is highly coupled to Chl-a concentration under normal circumstances for turbid waters since the cooling rate is inversely proportional to the trophic state of the lake. A ratio between the WST between two neighborhood points *A* and *B* is given by

$$\Delta \mathrm{WST}_A / \Delta \mathrm{WST}_B \approx d_B / d_A \tag{1}$$

where ΔWST is the surface temperature change, and d_A and d_B are the Chl-a concentration of the two neighborhood points.

To determine a set of factors for constructing a robust downscaling model, a two-stage procedure was applied to implement optimal factor selection. First, we used the significance assessment approach to evaluate the contribution of the abovementioned auxiliary factors. Second, according to the significance-ranked results, the stepwise regression method [49] was used to avoid factor multicollinearity in downscaling. The subset of factors with the highest accuracy was used as the best explanatory factor for the model.

In addition, we differentiate the roles of the six different types of auxiliary factors and find out the best factors to facilitate the Chl-a downscaling, by designing eight sets of factor combinations for the downscaling. These combinations are as follows.

1) Multispectral reflectance.
2) Multispectral reflectance + Chlorophyll indices.
3) Multispectral reflectance + Red-edge indices.
4) Multispectral reflectance + TF.
5) Multispectral reflectance + TC.
6) Multispectral reflectance + backscattering characteristics.
7) All factors.
8) Optimal factors.

C. Step 3: Construction of Downscaling Model

Several studies have discussed ML algorithms (such as RF) for solving nonlinear regression problems in downscaling [50],

[51], [52]. Unlike other ML algorithms, GBDT structures an aggregate of decision tree learners by using boosted iterations. At every iteration, a new decision tree is used to reinforce a loss function based on the sharpest gradients. The GBDT method has several unique properties other ML algorithms miss. One of them is that the GBDT is more stable to offsets and imbalances. Thus, a high and efficient predictive property is assured in the model [53]. Given the complex nonlinear relations between Chl-a concentration and its features, the GBDT algorithm was selected to construct the downscaling model.

Downscaling methods are mostly based on the scale invariance hypothesis. This hypothesis states that the statistical relation between predictors and coarse-resolution explanatory factors also holds at fine-resolution [28], [54], [55]. The specific procedures for the downscaling are as follows. First, the statistical relation between the explanatory factor and original coarse-resolution Chl-a concentration was established using the GBDT regression model. Then, based on the constructed statistical relation, the explanatory factors at fine and coarse resolution were applied to predict the Chl-a concentration at fine and coarse resolution, respectively. Finally, the difference between the coarse resolution and the original coarse resolution Chl-a concentration is considered to be the fine resolution Chl-a concentration prediction via using the Kriging. Mathematically, it is expressed as

$$\mathrm{CHL}_f = \mathrm{CHL}_c + \left(F_c\left(S_f\right) - F_c\left(S_c\right)\right) \tag{2}$$

where *f* and *c* represent fine and coarse resolution, respectively, and *F* represents the statistical function between Chl-a concentration and explanatory factor (*S*).

There are three important parameters in the GBDT downscaling method: the number of decision trees in the regression procedure, the explanatory factors used to segment the nodes, and the loss function. The parameterization of downscaling models is critical to avoid multicollinearity and overfitting. In this work, we adopted a two-stage procedure to implement model parameterization. For the first stage, inspired by Zebari et al. [56], the significant assessment and stepwise regression were used to select explanatory factors and deal with multicollinearity since they preserved the physical meaning of the factors for subsequent analysis. For the second stage, a grid search method with ten-fold cross-validation (i.e., dividing all pixels into ten groups; nine groups at a time for training and the rest for validation) [57] was applied to determine the number of decision trees and the loss function. Ultimately, 100 and the minimum absolute deviation were determined as the final number of decision trees and the loss function, respectively.

D. Step 4: Accuracy Verification Strategy

Due to the lack of the Chl-a concentration observed at high spatial resolutions, the aggregation-disaggregation approach was adopted to evaluate model performance [50], [58], [59]. Specifically, we maintained the original Chl-a concentration (300 m) to auxiliary factor (30 m) spatial resolution ratio of 10:1. Initially, Chl-a concentration and explanatory factors were up to 3000 m and 300 m, respectively, where the original 300-m Chl-a concentration was used as a reference to validate the 3000 m downscaled Chl-a concentration.

Statistical analyses were also performed on a series of quantities: the determination of the coefficient (R^2), root mean squared error (RMSE), mean absolute error (MAE), and structural similarity (SSIM). R^2 represents the variance explained by the model; RMSE is the most commonly-used statistical term to quantify the model error, revealing the deviation between the predicted and the true values; MAE is the average value of absolute errors, which provides an alternative way for analysis of the prediction errors; SSIM represents the SSIM between the downscaled and original images. These indicators can be expressed as follows:

$$R^2 = 1 - \frac{\sum_{i=1}^{m}\left(\mathrm{CHL}_c - \mathrm{CHL}_f\right)^2}{\sum_{i=1}^{m}\left(\mathrm{CHL}_c - \mu_f\right)^2} \tag{3}$$

$$\mathrm{RMSE} = \sqrt{\frac{1}{m}\sum_{i=1}^{m}\left(\mathrm{CHL}_c - \mathrm{CHL}_f\right)^2} \tag{4}$$

$$\mathrm{MAE} = \frac{1}{m}\sum_{i=1}^{m}\left|\left(\mathrm{CHL}_c - \mathrm{CHL}_f\right)\right| \tag{5}$$

$$\mathrm{SSIM} = \frac{\left(2\mu_c\mu_f + C_1\right)\cdot\left(2\sigma_{cf} + C_2\right)}{\left(\mu_c^2 + \mu_f^2 + C_1\right)\cdot\left(\sigma_c^2 + \sigma_f^2 + C_2\right)} \tag{6}$$

where m is the number of samples, the subscripts c and f denote coarse and fine resolution, μ is the average of the Chl-a concentration, σ^2 and μ^2 are the covariance and variance of Chl-a concentration, and C_1 and C_2 are constants used to maintain numerical stability, which are set to 0.1 and 0.05, respectively.

IV. Results and Analysis

A. Optimal Combination of Explanatory Factors

The individual significance of each auxiliary factor and the variation of downscaling accuracy with the factors are shown in Fig. 3. The most significant two explanatory factors are NDCI and WST, possessing factor significant scores of 16.5% and 11.5%, respectively. This is because when the Chl-a (e.g., phytoplankton) presents in water, more NIR is reflected and more red light is absorbed, leading to a significant increase in NDCI [44]. Concurrently, all the lakes in the study area exhibited a large nutrient state (see Table IV), indicating that there would be potential coupling existed between NDCI and Chl-a concentration in lakes with larger trophic contrasts across the water surface. In addition, the warm temperature provides the basic conditions for phytoplankton blooms in the water body, and therefore WST can sharply affect the changes in Chl-a concentration [48].

As shown in Fig. 3, with an increasing number of auxiliary factors involved in the downscaling, the R^2 increased significantly from 32.5% to 75.8% in the first stage (only six factors). This increment is in response to the high importance score of the auxiliary factors and the low correlation between factors (the maximum correlation coefficient is 0.67, see Fig. 10 in the appendix for details). In the middle stage (7–14 factors),

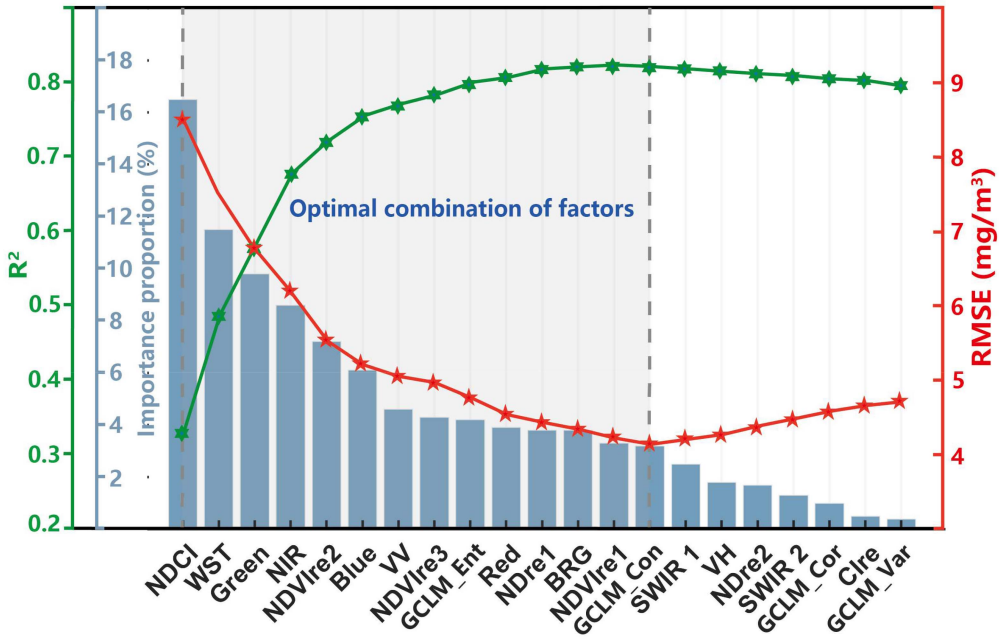

Fig. 3. Individual importance of each auxiliary factor and the variation of downscaling accuracy with factors.

the speed of R^2 improvement decreased significantly but still showed a steady upward trend, and the R^2 gradually reached 75.8%. In the later stages (15–21 factors), the R^2 gradually showed a decreasing trend. This is because of the increase of redundant factors and irrelevant factors in the later stages (see Fig. 10). Therefore, the first 14 factors would be the optimal feature set, specifically, they are NDCI, WST, Green, NIR, NDVIre2, Blue, VV, NDVIre3, GCLM_Ent, Red, NDre1, BRG, NDVIre1, and GCLM_Con.

B. Comparison of Different Types of Auxiliary Factors

To quantitatively and accurately assess the effects of different types of factors on the downscaling accuracy, the analysis of the accuracy assessment was carried out for different combinations. R^2 and RMSE are included in the main evaluation indices, and the specific results are presented in Fig. 4. Based on the multispectral reflectance, the mean R^2 and RMSE were 75.42% and 7.94 mg/m^3, respectively. When different types of factors are added to the multispectral reflectance, the downscaling accuracy is shown to be varying (see Fig. 4). The downscaling accuracy tends to increase with the addition of chlorophyll index, red-edge index, thermal features, and backscattering features. There is a significant increase in accuracy for the chlorophyll index and red-edge index (p<0.01). However, the downscaling accuracy tends to decrease with the addition of TF, with a mean R^2 of 73.11% and RMSE of 8.04 mg/m^3. This indicates that factors related to biochemical components of phytoplankton (e.g., chlorophyll index, red-edge index, etc.) can effectively infer the spatial variability of Chl-a concentrations, whereas image TF limits their extraction of information on Chl-a concentrations in diverse environments due to their nonsmooth nature. In addition,

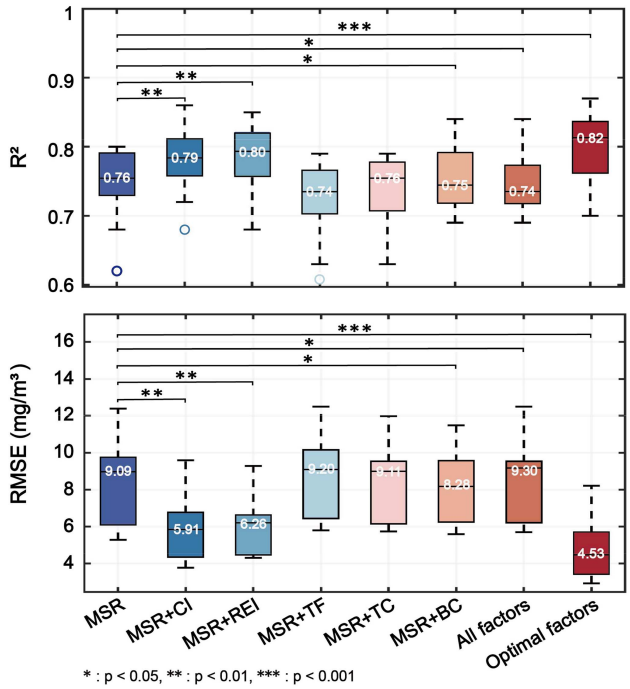

Fig. 4. Boxplot of R^2 and RMSE for seven combinations over Lakes 1–12. The Wilcoxon test was applied to assess whether there was a significant difference in accuracy between the referenced combination and the other combinations. MSR: multispectral reflectance, CI: chlorophyll index, REI: red-edge index, TF: texture feature, TC: thermal characteristic, BC: backscattering characteristic.

when all features were involved in downscaling, accuracy decreases, which may be due to the presence of redundancy from multiple covariates between factors.

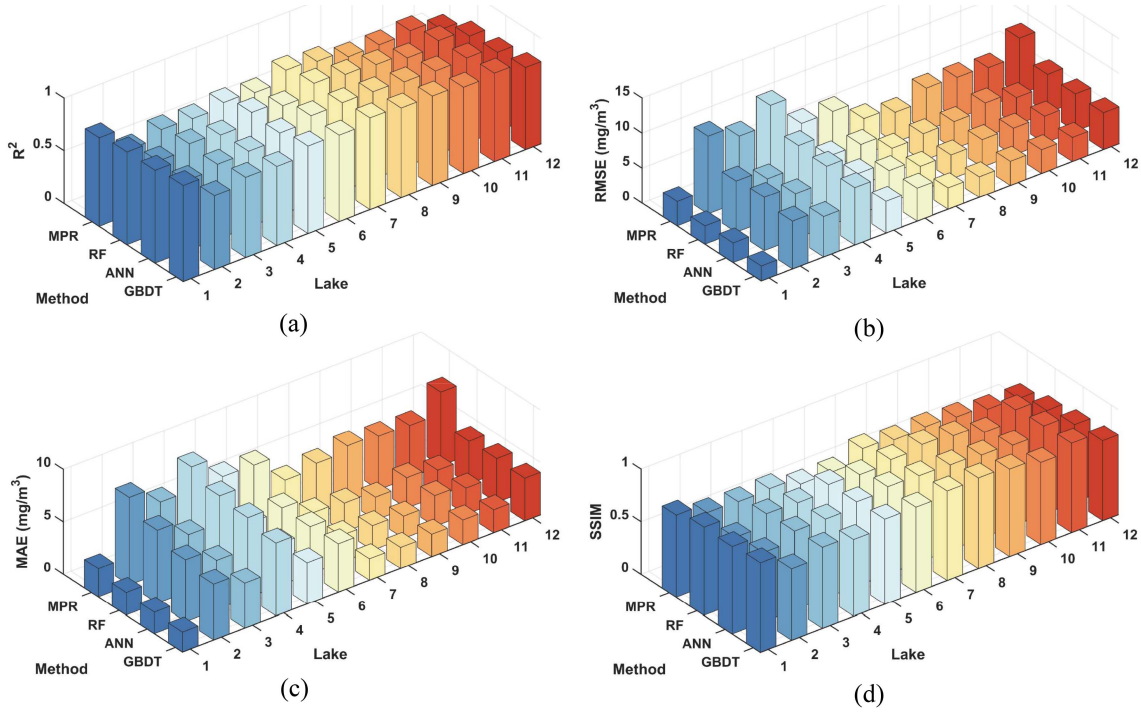

Fig. 5. Downscaling accuracy assessment depicted as 3-D histograms for the four different approaches for Lakes 1–12. (a) R^2. (b) RMSE. (c) MAE. (d) SSIM.

C. Comparison of Diverse Regression Models

To assess the performance of the GBDT method based on MVA, three alternatives (the MPR, RF, and ANN) based on the same inputs, were implemented for intermethod comparison. The accuracies of Chl-a concentration downscaling contributed by each method are shown in Fig. 5 as individual 3-D histograms in terms of the statistical quantities. As can be seen from Fig. 5, the GBDT consistently delivered the best results in diverse lakes, outperforming the ANN, RF, and MPR. Compared to the MPR approach, the downscaling RMSEs of the GBDT method correspond to a 31% to 39% improvement. The ANN and RF methods were less accurate than GBDT but still had a 5% to 25% improvement over the MPR approach.

The statistics derived from different methods are tabulated in Table II. In a brief comparison of 12 lakes, GBDT has the highest accuracy (average R^2 is 0.82, RMSE is 4.47 mg/m^3), followed by ANN (average R^2 is 0.79, RMSE is 4.99 mg/m^3), RF (average R^2 is 0.77, RMSE is 5.11 mg/m^3), and MPR (average R^2 is 0.71, RMSE is 7.22 mg/m^3).

For some lakes, the discrepancy in performance between the methods is significant. For example, in Lake 1 (June 2021) and 4 (September 2021), the difference in RMSE between the GBDT and MPR methods was the largest among all the lakes in the study area. For the Chl-a concentration of Lake 4 acquired in September, the downscaling accuracy of GBDT was higher relative to the MPR based on uniform decomposition. This may be attributed to accelerated changes in the phytoplankton status of the lake during the late rainy season [60]. This is expected that the subpixel changes resulting from the uniform decomposition cannot reproduce for large 300-m pixels.

The pixel-based density scatter plots for the methods are shown in Fig. 6. As can be seen in the scatter plots, the points concentrated more for GBDT compared to others. However, ANN and GBDT are comparable for some extreme observations. The scatter plots of the GBDT and ANN are equipollent for some lakes (e.g., Lake 6 and Lake 10), also they show that GBDT and ANN have outperformed the RF and MPR methods. This is consistent with the accuracy shown in Table II.

As can be seen in Fig. 7, the GBDT, ANN, RF, and MPR methods reproduced most of the contrasts in the spatial distribution of Chl-a concentration when compared to the original maps. In addition, the downscaled Chl-a concentration maps generated by the GBDT method showed higher agreement with the hues of the original maps, compared with the ANN, RF, and MPR methods. This indicates that the GBDT algorithm better recovered the original spatial variability of Chl-a concentration. For some lakes (e.g., Lake 1), the downscaled Chl-a concentration maps generated by the MPR method possess more overestimation. For the fine-resolution, Chl-a concentration maps generated by GBDT, ANN, and RF methods, similar overestimations were much less significant, especially, by the GBDT method. This suggests that GBDT, ANN, and RF methods can better capture extreme Chl-a concentration variation at the subpixel level, still, the GBDT method is shown to be superior to the ANN and RF methods for such applications.

The above-discussed results also suggest that the fine-resolution images obtained from the GBDT method have high consistency with the original images, and the RMSE and R^2 are both satisfactory (mean RMSE under 4.50 mg/m^3 and R^2 over 0.80). This indicates that the proposed MVA-GBDT method can

TABLE II
STATISTIC RESULTS OF THE GBDT, ANN, RF, AND MPR METHODS

Lake	GBDT				ANN				RF				MPR			
	R^2	RMSE/ $mg \cdot m^{-3}$	MAE/ $mg \cdot m^{-3}$	SSIM	R^2	RMSE/ $mg \cdot m^{-3}$	MAE/ $mg \cdot m^{-3}$	SSIM	R^2	RMSE/ $mg \cdot m^{-3}$	MAE/ $mg \cdot m^{-3}$	SSIM	R^2	RMSE/ $mg \cdot m^{-3}$	MAE/ $mg \cdot m^{-3}$	SSIM
1	0.91	2.12	1.89	0.85	0.88	2.79	2.01	0.83	0.88	2.61	2.17	0.84	0.84	3.48	2.71	0.78
2	0.70	6.82	5.31	0.68	0.67	7.62	5.91	0.66	0.68	7.33	6.98	0.63	0.62	11.11	8.36	0.69
3	0.76	5.77	4.27	0.77	0.71	6.43	4.72	0.75	0.73	5.94	5.42	0.74	0.69	9.42	6.78	0.68
4	0.75	8.21	6.98	0.73	0.72	8.65	7.65	0.75	0.7	8.99	7.98	0.73	0.68	12.09	8.99	0.69
5	0.83	4.53	3.96	0.81	0.78	5.89	4.01	0.80	0.80	5.81	4.31	0.79	0.72	7.82	6.93	0.62
6	0.82	4.72	4.63	0.81	0.83	4.61	4.52	0.83	0.75	5.73	4.56	0.77	0.70	7.81	6.88	0.62
7	0.87	3.06	2.07	0.85	0.84	3.52	2.54	0.82	0.85	3.48	2.97	0.80	0.80	5.09	4.32	0.73
8	0.85	2.93	2.01	0.86	0.83	3.44	2.34	0.81	0.82	3.85	2.74	0.83	0.77	4.28	4.78	0.70
9	0.85	3.44	2.13	0.83	0.81	3.92	2.11	0.79	0.80	3.87	2.17	0.80	0.70	6.02	5.32	0.71
10	0.82	3.38	2.35	0.78	0.80	3.84	2.92	0.77	0.75	4.82	2.88	0.72	0.70	5.85	5.09	0.69
11	0.84	3.43	2.18	0.85	0.81	3.85	2.50	0.84	0.80	3.88	2.46	0.82	0.72	5.52	4.98	0.65
12	0.78	5.25	4.05	0.76	0.75	5.32	4.18	0.74	0.73	5.48	4.09	0.70	0.62	8.09	7.03	0.64
average	0.82	4.47	3.48	0.81	0.79	4.99	3.78	0.78	0.77	5.15	4.06	0.76	0.71	7.22	6.01	0.68

feasibly increase the spatial resolution of Chl-a concentration. However, its performance can be hindered in some cases. For example, Lakes 2 and 4 have high RMSEs (exceeding 6.5 mg/m^3). Such limited performance can be explained in terms of the following reasons.

1) Limited spatial resolution of the satellite imagery: Although the Sentinel-2 imagery has a resolution of 10 m, such a resolution is still inadequate for the inversion of water surfaces less than 100 m wide (i.e., these surfaces can be captured with only a few pixels), particularly for the extraction of boundaries. To reduce the downscaling errors in the boundaries, this study extracted lake boundaries as finely as possible from supplementary high-resolution images simultaneously to relieve the problem. However, as an additional high-resolution image source is required, a complete remedy is impossible.
2) High temporal variability of Chl-a concentration: The Chl-a concentration is unstable and susceptible to fluctuations in the water environment, so it can vary considerably over short periods of time even for small areas [61], [62]. Therefore, we conducted model training using Chl-a concentration from multiple regions at different times. However, this can only ensure high-accuracy prediction for most regions, and low prediction accuracy is still inevitably found for some regions with high water quality heterogeneity and large temporal variability in Chl-a concentration.
3) Impact caused by other nonmodeled factors: The factors that influence the distribution of Chl-a concentration are dominated by hydrologic and meteorological factors, with other environmental factors, such as runoff and topography. It is evident from field studies, for example, that water depths have deepened substantially over time in some areas such as Lake 7 and Lake 8 [63]. Not only does this affect the actual Chl-a concentration in the lakes, but also reduces the accuracy of satellite-derived Chl-a concentration. Thus, it may be beneficial to incorporate more related factors to further improve the model.

Overall, the proposed MVA-GBDT downscaling method, incorporating different types of auxiliary factors, yielded high consistency between the downscaled outcomes and original values, suggesting that the downscaled outcomes can be used as a reference for the subsequent spatiotemporal analysis of Chl-a concentration with fine spatial resolution.

D. Performance of the MVA-GBDT Method in Different Environments

Training models with complex features tend to be prone to overfitting issues (i.e., the model fits well only in certain regions), then model generalization may be limited. To verify if the proposed MVA-GBDT model suffers from overfitting, a cross-validation experiment of downscaling models is performed. The MVA-GBDT model trained with data obtained from a single

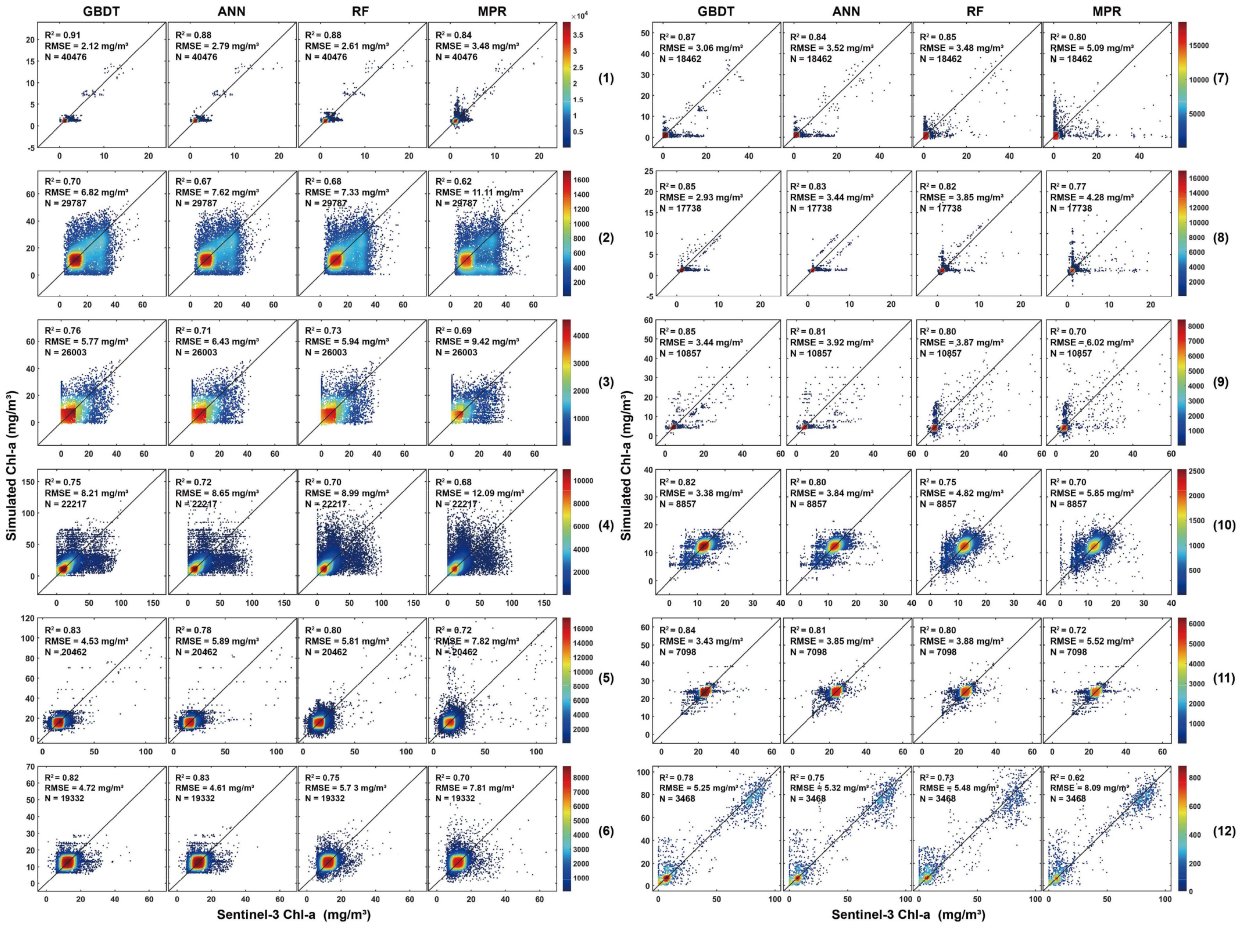

Fig. 6. Pixel-based density scatterplots of Sentinel-3 Chl-a versus downscaled Chl-a at 300-m resolution by employing GBDT, ANN, RF, and MPR for Lakes 1–12.

lake, is used for downscaling prediction for the rest of the lakes in the study area. The audits were conducted over different time periods for the 12 lakes.

The training and test results for the 12 lakes based on the MVA-GBDT model, are shown in Table III. Each row in the table represents the MVA-GBDT model trained with the data from an individual lake, and each column represents the results of testing the trained MVA-GBDT model. The smallest RMSE is 3.10 mg/m^3 for Lake 1, and it is relatively larger for Lake 2 (7.83 mg/m^3) and Lake 4 (8.75 mg/m^3). Factors affecting the results are derived from several sources. The most important part of which is the difference in the surrounding environment for the lakes as well as the quality of the data and the correlation between the training and reference data.

Lake 2 is located in the middle and lower reaches of the Yangtze River, as can be seen in Fig. 1, which has the greatest difference in width between the 12 lakes. Meanwhile, Lake 4 lies on the border of the developed provinces and towns, which is the most severely nutrient-rich among the 12 lakes (water blooms occur frequently in summer). Because these conditions and natural factors of Lakes 2 and 4 are very distinct from that of other lakes, the RMSE differences are relatively larger for local downscaling.

By comparing the downscaled results obtained after training the MVA-GBDT on the remaining Lakes, the RMSEs of test scores using the training data confined within their surface area, are the smallest, with the exception of two special study regions (e.g., Lakes 5 and 7). The best results from Lakes 5 and 7 are with the 8th and 9th training models, respectively. It is seemingly that this phenomenon occurs because explanatory variables in the study area itself are not sufficiently well adjusted for surface temperature, and rather than the best model test results are obtained under the training of study regions more similar to them. The difference between the RMSE and the optimal results is 0.57 mg/m^3 for Lake 5 and 0.81 mg/m^3 for Lake 7. It is worth noting that there is no large difference found from the MVA-GBDT model built using its own study region as training data for this case. Consequently, the proposed MVA-GBDT method is shown able to be generalized for downscaling of Chl-a concentration in a wide variety of inland lakes.

V. Discussions

A. *Chl-a Concentration Downscaling From 300 to 30 m*

As it is virtually impossible to collect high-resolution Chl-a concentrations across multiple study areas nationwide to directly validate downscaled Chl-a concentrations (30 m) from

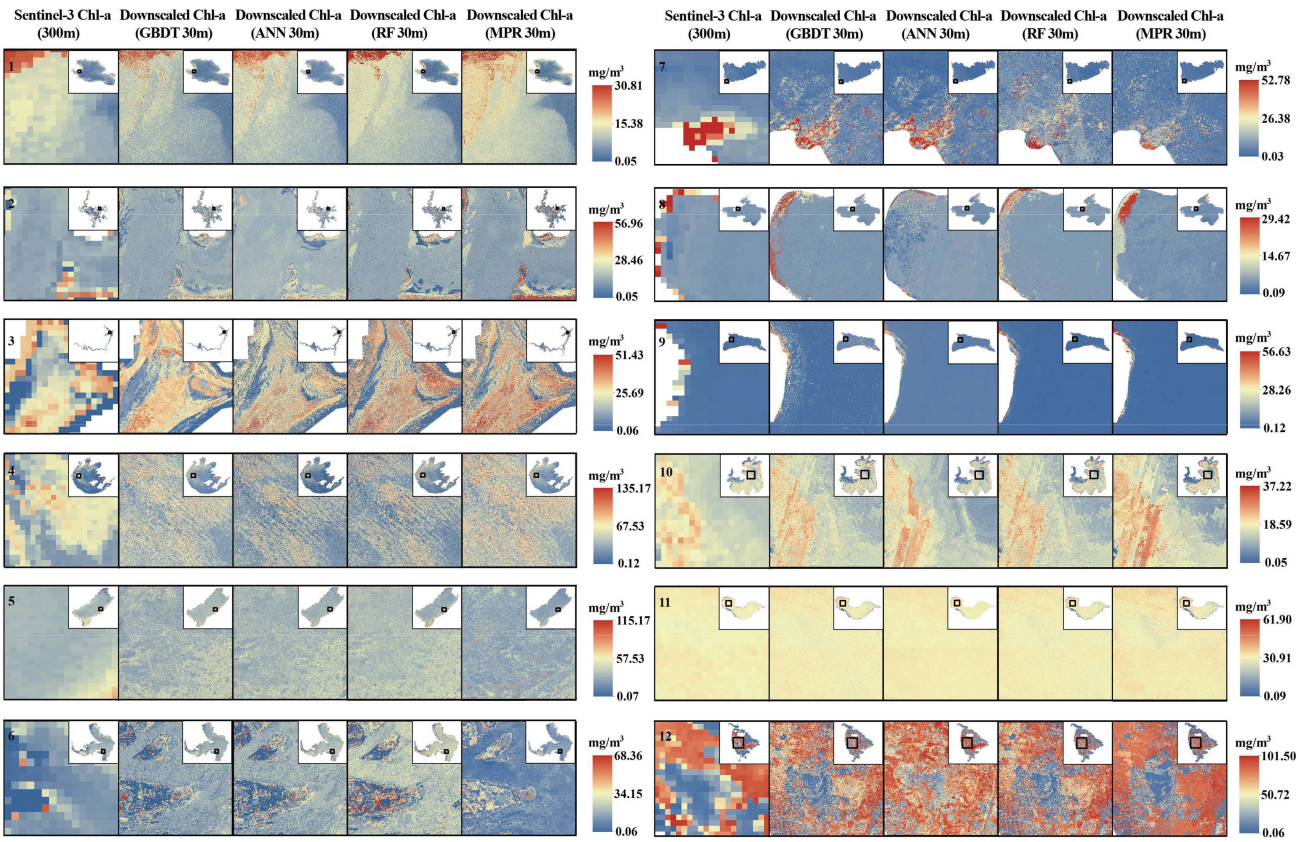

Fig. 7. Downscaled Chl-a concentration map using GBDT, ANN, RF, and MPR for Lakes 1–12.

TABLE III
DOWNSCALING ERROR STATISTICS FOR PROPOSED METHOD TRAINED ON EACH AREA AT DIFFERENT TIME

Data date	Lake No.	The test results of RMSEs for distinct 12 lakes in China (mg/m³)											
		1	2	3	4	5	6	7	8	9	10	11	12
2021-12-11	1	**3.10**	8.41	6.83	9.15	5.69	5.89	4.58	5.28	5.19	4.33	4.73	5.83
2021-07-22	2	3.82	**7.83**	6.93	9.02	5.75	6.12	4.07	4.37	4.97	4.42	4.79	5.92
2021-09-21	3	4.78	8.33	**6.37**	9.54	5.76	5.97	4.65	4.42	5.24	4.38	4.87	6.25
2021-03-02	4	3.25	8.81	6.72	**8.75**	5.83	6.03	4.47	3.68	5.52	4.35	4.31	6.31
2021-01-04	5	3.56	9.99	6.45	9.34	4.78	6.14	4.02	3.61	5.61	4.29	4.56	6.17
2021-05-08	6	4.52	8.35	6.84	9.62	5.13	**4.52**	3.87	3.45	5.38	4.72	4.51	6.59
2021-02-01	7	3.91	8.48	6.95	9.86	5.32	5.54	3.37	3.75	5.28	4.31	4.65	6.71
2021-09-11	8	3.95	8.88	7.02	9.89	**4.11**	5.81	3.75	**2.76**	4.32	4.65	4.34	6.66
2021-10-25	9	4.24	8.52	6.95	9.53	5.21	5.48	**2.56**	4.15	**3.44**	4.69	4.26	6.75
2021-06-24	10	4.25	9.41	6.98	9.39	5.06	5.77	3.57	4.81	4.15	**3.75**	4.01	5.87
2021-04-18	11	4.04	9.72	7.09	9.42	5.77	6.09	3.46	3.82	4.65	4.98	**3.56**	5.98
2021-11-17	12	5.33	8.86	7.14	9.45	5.45	6.01	3.69	4.39	5.34	4.54	3.96	**5.09**

The numbers marked in bold are the best results produced by this framework.

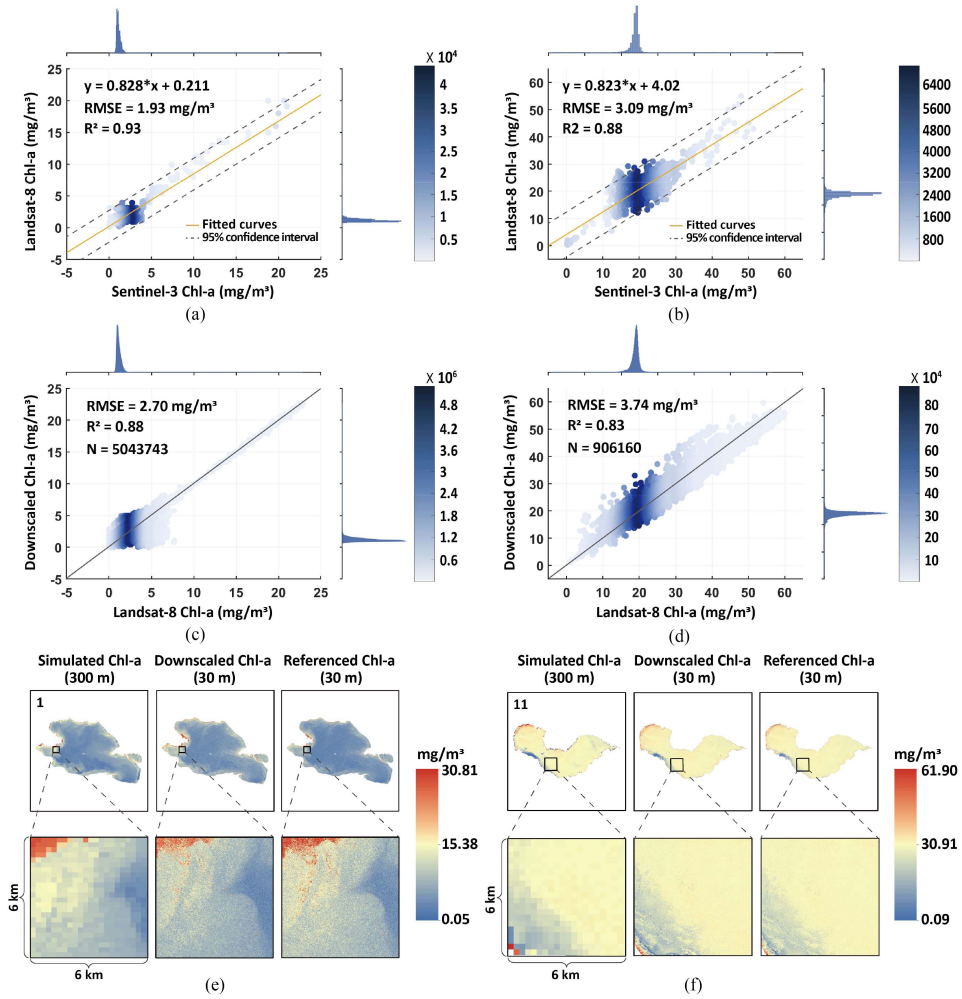

Fig. 8. Downscaling Chl-a concentration from 300 to 30 m. (a) and (b) Scatter distribution and linear fit of Sentinel and Landsat Chl-a concentrations for two lakes. (c) and (d) Pixel-based density scatterplots of Landsat Chl-a concentrations versus downscaled Chl-a at 30-m resolution by employing MVA-GBDT. (e) and (f) Downscaled Chl-a concentration map of Lake 1 and Lake 11.

Sentinel-3 Chl-a concentrations (300 m), we employed the widely popular "upscaling-downscaling" technique [50], [58], [59] for validation in this research. Specifically, the original 300-m Sentinel-3 Chl-a concentrations were first upscaled to 3000 m. Subsequently, the 3000-m Sentinel-3 Chl-a concentration was downscaled to 300 m by applying the MVA-GBDT method and then compared to the reference 300 m Chl-a concentration.

We also recognize that this "upscaling-downscaling" technique from 3000- to 300-m smooths out the spatial heterogeneity of satellite images, which may lead to results based on this technique that differ from the true Chl-a concentrations downscaled from 300 to 30 m. Therefore, two images (Lake 1 and Lake 11) of Chl-a concentration from Landsat-8 [65] with a spatial resolution of 30 m was collected, and the performance of the MVA-GBDT method was examined by downscaling Chl-a concentrations from 300 to 30 m.

Fig. 8(a) and (b) depicts the scatter plot and linear regression relationship between Sentinel and Landsat Chl-a concentration products for the two substudy areas at the coarse spatial resolution level. As shown in Fig. 8(a) and (b), the coefficients of determination for the Sentinel and Landsat Chl-a concentrations reach 0.93 and 0.88 at the 95% confidence interval, respectively, with the RMSE controlled below 3.50 mg/m^3. This high correlation suggests that the Landsat Chl-a concentration products can be used as validation data for the downscaling results of the Sentinel Chl-a concentrations.

The pixel-based density scatterplots of Landsat-8 Chl-a concentrations versus downscaled Chl-a concentrations at 30-m resolution using the MVA-GBDT method in the two lakes are shown in Fig. 8(c) and (d). Although these evaluations are slightly different from those from 3000 to 300 m, the main results are similar. For the different inland lakes, the MVA-GBDT downscaling algorithm all achieved satisfactory results with mean RMSE below 4.00 mg/m^3 and R^2 above 0.80. We further demonstrate the performance of MVA-GBDT in Chl-a concentrations downscaling from 300 to 30 m [see Fig. 8(e) and (f)]. The results show that MVA-GBDT downscaled Chl-a concentrations are able to maintain the overall spatial pattern of 300 m Chl-a

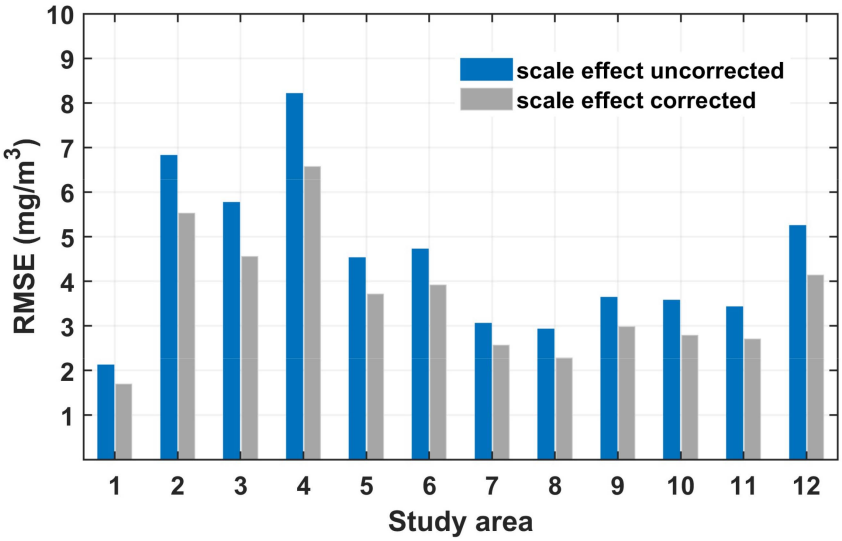

Fig. 9. RMSEs calculated using the proposed MVA-GBDT method of uncorrected and corrected scale effects.

concentrations and are also able to add abundant chlorophyll a concentration detail very similar to that of the reference Chl-a concentration [see Fig. 8(e) and (f)]. Furthermore, validations show that RMSEs for all Chl-a concentrations downscaled by MVA-GBDT are satisfactory in such heterogeneous lakes. This result guarantees that MVA-GBDT can be utilized in practical situations to downscale Sentinel Chl-a concentrations from 300 to 30 m.

B. Analysis of Scale Effect in the MVA-GBDT Method

As described in Section III-C, the Chl-a concentration downscaling methods assume the same statistical relationship exists between Chl-a concentration and auxiliary factors at various spatial resolutions. However, this scale-invariant statistical relationship is not always correct. For example, the relationship between Chl-a concentration and NDCI has been shown to vary with spatial resolution [44], and the relationship between Chl-a concentration and WST varies considerably at scale [64]. Therefore, this study further improved the downscaling results by considering scale effects.

The proposed MVA-GBDT method uses a comparison scheme to quantify the uncertainty caused by scale effects based on the availability of high-resolution Chl-a concentration obtained from Landsat-8, which was shown high consistency (as stated in Section V-A). The key to this scheme lies in the replacement of the statistical relationship between scale factors and Chl-a concentrations at low resolution [i.e., F_c (•) in (2)] with that at high resolution [hereafter referred to as F_f (•)]. With the high-resolution statistical relationship F_f (•), the standard downscaling process given in (2) can be modified as follows:

$$\mathrm{CHL}_f = \mathrm{CHL}_c + \left(F_f\left(S_f\right) - F_c\left(S_c\right)\right). \tag{7}$$

Equation (7) is interpreted similarly to (2). The scale effect is quantified by comparing the difference in accuracy obtained from (2) and (7).

Based on the above scheme, the scale effect of MVA-GBDT was quantified (see Fig. 9). The results suggest that taking the scale effect into account improves the accuracy of the proposed downscaling method. In several heterogeneous regions, the RMSEs after considering scale effects are significantly lower compared to those without scale effects, with a reduction of about 20%. This indicates that the precision of the proposed downscaling method can be higher when scale effects are taken into account.

C. Prospects of the Proposed Method

The presented MVA-GBDT method can facilitate the generation of Chl-a concentrations with a high spatial or temporal resolution for national lakes and related applications owing to the following properties.

1) High applicability to heterogeneous lakes: MVA-GBDT can directly downscale Sentinel-3 Chl-a concentrations to a resolution of 30 m, enhancing spatial details while preserving the spatial distribution of the original 300 m Chl-a concentration data, especially for lakes with high heterogeneity (see Fig. 7).
2) Nationwide generalization: MVA-GBDT is applicable nationwide due to feasibility testing under a variety of geographic lakes across the country and the regular and global coverage of Sentinel-3 observations.
3) Coupling with spatiotemporal fusion algorithms: MVA-GBDT has the potential to be coupled with spatiotemporal fusion algorithms to generate high spatiotemporal Chl-a concentration products with a resolution of 30 m.
4) Mutipurposes: MVA-GBDT method can provide continuous, fine-scale Chl-a concentration information on a large-scale using block processing, supporting a wide range of applications in lake ecology, eutrophication, fisheries management, biochemical cycling, etc.

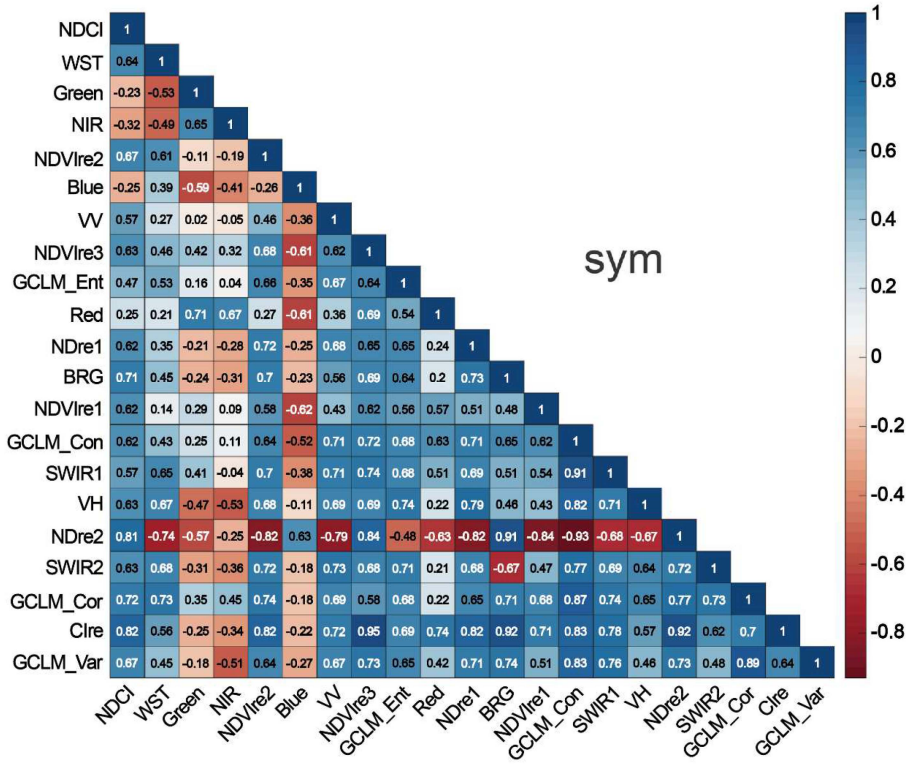

Fig. 10. Correlations between diverse auxiliary factors.

VI. Conclusion

Obtaining high-resolution and accurate lake Chl-a concentration derived from satellite imagery is important to many aquatic applications. In this article, we proposed a downscaling method based on the MVA and GBDT, namely MVA-GBDT, aiming to downscale Sentinel-3 Chl-a concentration from 300 to 30 m. Furthermore, we compared the performance of the presented method with two other classic methods (MPR and RF) for 12 different inland lakes with distinct characteristics in China. The main contributions of this article are summarized as follows.

1) The MVA-GBDT method for downscaling Chl-a concentration for inland lakes is proposed. It is based on the MVA and GBDT regression methods, which outperformed the other two methods (RF, MPR) for downscaling at distinct lake environments. The performance of the method is guaranteed by the optimal assessment of spatial weights inserted by the GBDT method for Chl-a concentration and the integration of the optimal set of auxiliary factors into the regression. Analysis of the statistical indicators showed that the proposed MVA-GBDT method delivers an average RMSE of 4.505 mg/m^3, an improvement in accuracy of between 5% and 39% compared to the other methods shown in this article.
2) High rigor of the MVA-GBDT method is demonstrated and analyzed. The proposed method can be generalized to downscale Chl-a concentration under different conditions, achieving an average RMSE of 5.371 mg/m^3 after cross-validation for more than ten distinct inland lakes. The resultant accuracy difference is less than 0.900 mg/m^3. The results could potentially contribute to the analysis of bio-geophysical mechanisms in inland lake environments.
3) Multiple types of auxiliary factors (multispectral reflectance, chlorophyll index, red-edge index, TF, TC, and backscattering characteristic) are first integrated into the GBDT method, which optimizes the method to deliver the best outcome for such an application. It is shown that the NDCI and WST were dominant factors for the downscaling, particularly the NDCI of the lakes with a relatively larger nutrient variation. The results are expected to serve as a reference for the analysis of the bio-physical mechanism in the trophic environment.

In conclusion, our results reveal that the performance of the proposed MVA-GBDT method is promising with the addition of satellite and *in situ* measurements, downscaling methods should be further explored in the future, and the proposed method may be upgraded to downscale data further to 10 m. For example, the inclusion of the temporal variation of Chl-a concentration within the method could be viewed as providing a high spatiotemporal resolution product of Chl-a concentration.

Appendix

See Appendix Fig. 10 and Table IV.

TABLE IV
OUTLINE OF 12 LAKES

No.	Lake name	Longitude, Latitude	Date	Climate zone	Area (km^2)	Mean Depth (m)	Lake type	Lake conditions
1	Qinghai	100°16′34″, 36°47′58″	2021-06-09	Warm temperate	4456	18.61	Saltwater	Eutrophic [66]
2	Poyang	116°18'40", 29°19'43"	2021-01-12	Subtropical	4070	8.40	Freshwater	Mesotrophic [67]
3	Dongting	112°25′05″, 29°03′45″	2021-02-19	Subtropical	2820	6.41	Freshwater	Mesotrophic [67]
4	Tai	120°12′01″, 33°23′05″	2021-09-28	Subtropical	2428	2.12	Freshwater	Eutrophic [67]
5	Hulun	117°26′25″, 48°58′27″	2021-07-31	Mid-temperate	2043	5.75	Freshwater	Eutrophic [68]
6	Hongze	118°31′08″, 25°48′12″	2021-11-30	Warm temperate	2069	1.52	Freshwater	Eutrophic [67]
7	Namuco	90°09′30″, 30°32′35″	2021-08-31	Plateau climatic	1940	34.84	Saltwater	Oligotrophic [63]
8	Silinco	88°32′50″, 32°40′12″	2021-03-31	Plateau climatic	1650	30.20	Saltwater	Oligotrophic [63]
9	Bositeng	87°12′20″, 42°10′02″	2021-04-29	Plateau climatic	1646	8.15	Freshwater	Oligotrophic [69]
10	Gaoyou	120°23′55″, 36°04′57″	2021-12-27	Subtropical	1005	5.56	Freshwater	Eutrophic [67]
11	Chao	117°30′14″, 31°36′28″	2021-10-24	Subtropical	2046	2.89	Freshwater	Eutrophic [67]
12	Weishan	124°05′46″, 45°00′35″	2021-05-27	Mid-temperate	1266	1.58	Freshwater	Eutrophic [70]

ACKNOWLEDGMENT

The authors are grateful to the ESA for free access to the Sentinel-2 and Sentinel-3 data. They are also thankful to other institutions that provided the products required for this research.

REFERENCES

[1] Y. Vadeboncoeur and A. D. Steinman, "Periphyton function in lake ecosystems," *Sci. World J.*, vol. 2, pp. 1449–1468, 2002, doi: 10.1100/tsw.2002.294.

[2] S. Tao et al., "Changes in China's lakes: Climate and human impacts," *Nat. Sci. Rev.*, vol. 7, no. 1, pp. 132–140, 2020, doi: 10.1093/nsr/nwz103.

[3] R. I. Woolway et al., "Global lake responses to climate change," *Nature Rev. Earth Environ.*, vol. 1, no. 8, pp. 388–403, 2020, doi: 10.1038/s43017-020-0067-5.

[4] S. Wang et al., "Trophic state assessment of global inland waters using a MODIS-derived Forel-Ule index," *Remote Sens. Environ.*, vol. 217, pp. 444–460, 2018, doi: 10.1016/j.rse.2018.08.026.

[5] J. Katz et al., "Chlorophyll function in the photosynthetic reaction center," *Annu. Rev. Biophys. Bioeng.*, vol. 7, no. 1, pp. 393–434, 1978, doi: 10.1146/annurev.bb.07.060178.002141.

[6] C. T. Filstrup and J. A. Downing, "Relationship of chlorophyll to phosphorus and nitrogen in nutrient-rich lakes," *Inland Waters*, vol. 7, pp. 385–400, 2017, doi: 10.1080/20442041.2017.1375176.

[7] P. Bierman et al., "A review of methods for analyzing spatial and temporal patterns in coastal water quality," *Ecol. Indicators*, vol. 11, no. 1, pp. 103–114, 2011, doi: 10.1016/j.ecolind.2009.11.001.

[8] J. Li et al., "A review of remote sensing for environmental monitoring in China," *Remote Sens.*, vol. 12, no. 7, 2020, Art. no. 1130, doi: 10.3390/rs12071130.

[9] P. J. Werdell et al., "Regional and seasonal variability of chlorophyll-a in Chesapeake Bay as observed by SeaWiFS and MODIS-Aqua," *Remote Sens. Environ.*, vol. 113, no. 6, pp. 1319–1330, 2009, doi: 10.1016/j.rse.2009.02.012.

[10] M. Kahru, R. M. Kudela, C. R. Anderson, and B. G. Mitchell, "Optimized merger of ocean chlorophyll algorithms of MODIS-Aqua and VIIRS," *IEEE Geosci. Remote Sens. Lett.*, vol. 12, no. 11, pp. 2282–2285, Nov. 2015, doi: 10.1109/LGRS.2015.2470250.

[11] Z. Cao et al., "A machine learning approach to estimate chlorophyll-a from Landsat-8 measurements in inland lakes," *Remote Sens. Environ.*, vol. 248, 2020, Art. no. 111974, doi: 10.1016/j.rse.2020.111974.

[12] J. Chen et al., "Remote estimation of colored dissolved organic matter and chlorophyll-a in lake Huron using Sentinel-2 measurements," *J. Appl. Remote Sens.*, vol. 11, no. 3, 2017, Art. no. 036007, doi: 10.1117/1.JRS.11.036007.

[13] W. W. Gregg and N. W. Casey, "Sampling biases in MODIS and SeaWiFS ocean chlorophyll data," *Remote Sens. Environ.*, vol. 111, no. 1, pp. 25–35, 2007, doi: 10.1016/j.rse.2007.03.008.

[14] M. Shen et al., "Determination of the downwelling diffuse attenuation coefficient of lake water with the Sentinel-3A OLCI," *Remote Sens.*, vol. 9, no. 12, 2017, Art. no. 1246, doi: 10.3390/rs9121246.

[15] K. Xue et al., "Inversion of inherent optical properties in optically complex waters using Sentinel-3A/OLCI images: A case study using China's three largest freshwater lakes," *Remote Sens. Environ.*, vol. 225, pp. 328–346, 2019, doi: 10.1016/j.rse.2019.03.006.

[16] G. H. Tilstone et al., "Performance of ocean colour chlorophyll a algorithms for Sentinel-3 OLCI, MODIS-Aqua and Suomi-VIIRS in open-ocean waters of the Atlantic," *Remote Sens. Environ.*, vol. 260, 2021, Art. no. 112444, doi: 10.1016/j.rse.2021.112444.

[17] C. Brockmann et al., "Evolution of the C2RCC neural network for Sentinel 2 and 3 for the retrieval of ocean colour products in normal and extreme optically complex waters," in *Proc. Living Planet Symp.*, 2016, vol. 740, pp. 54–59.

[18] B. Bechtel et al., "Downscaling land surface temperature in an urban area: A case study for Hamburg, Germany," *Remote Sens.*, vol. 4, no. 10, pp. 3184–3200, 2012, doi: 10.3390/rs4103184.

[19] S. Bonafoni, "Downscaling of Landsat and MODIS land surface temperature over the heterogeneous urban area of Milan," *IEEE J. Sel. Topics Appl. Earth Observ. Remote Sens.*, vol. 9, no. 5, pp. 2019–2027, May 2016, doi: 10.1109/JSTARS.2016.2514367.

[20] M. Bisquert et al., "Evaluation of disaggregation methods for downscaling MODIS land surface temperature to Landsat spatial resolution in Barrax test site," *IEEE J. Sel. Topics Appl. Earth Observ. Remote Sens.*, vol. 9, no. 4, pp. 1430–1438, Apr. 2016, doi: 10.1109/JSTARS.2016.2519099.

[21] F. Guo et al., "A new nonlinear method for downscaling land surface temperature by integrating guided and Gaussian filtering," *Remote Sens. Environ.*, vol. 271, 2022, Art. no. 112915, doi: 10.1016/j.rse.2022.112915.

[22] W. W. Immerzeel et al., "Spatial downscaling of TRMM precipitation using vegetative response on the Iberian Peninsula," *Remote Sens. Environ.*, vol. 113, no. 2, pp. 362–370, 2009, doi: 10.1016/j.rse.2008.10.004.

[23] C. Chen, S. Zhao, Z. Duan, and Z. Qin, "An improved spatial downscaling procedure for TRMM 3B43 precipitation product using geographically weighted regression," *IEEE J. Sel. Topics Appl. Earth Observ. Remote Sens.*, vol. 8, no. 9, pp. 4592–4604, Sep. 2015, doi: 10.1109/JSTARS.2015.2441734.

[24] Z. Shen and B. Yong, "Downscaling the GPM-based satellite precipitation retrievals using gradient boosting decision tree approach over Mainland China," *J. Hydrol.*, vol. 602, 2021, Art. no. 126803, doi: 10.1016/j.jhydrol.2021.126803.

[25] Y. Jing et al., "An attention mechanism based convolutional network for satellite precipitation downscaling over China," *J. Hydrol.*, vol. 613, 2022, Art. no. 128388, doi: 10.1016/j.jhydrol.2022.128388.

[26] O. Merlin et al., "A downscaling method for distributing surface soil moisture within a microwave pixel: Application to the Monsoon '90 data," *Remote Sens. Environ.*, vol. 101, no. 3, pp. 379–389, 2006, doi: 10.1016/j.rse.2006.01.004.

[27] M. Piles et al., "A downscaling approach for SMOS land observations: Evaluation of high-resolution soil moisture maps over the Iberian Peninsula," *IEEE J. Sel. Topics Appl. Earth Observ. Remote Sens.*, vol. 7, no. 9, pp. 3845–3857, Sep. 2014, doi: 10.1109/JSTARS.2014.2325398.

[28] Z. Wei et al., "Downscaling SMAP soil moisture estimation with gradient boosting decision tree regression over the Tibetan Plateau," *Remote Sens. Environ.*, vol. 225, pp. 30–44, 2019, doi: 10.1016/j.rse.2019.02.022.

[29] Y. Liu et al., "Generating high-resolution daily soil moisture by using spatial downscaling techniques: A comparison of six machine learning algorithms," *Adv. Water Resour.*, vol. 141, 2020, Art. no. 103601, doi: 10.1016/j.advwatres.2020.103601.

[30] Y. Fu et al., "Spatial downscaling of MODIS chlorophyll-a using Landsat 8 images for complex coastal water monitoring," *Estuarine, Coastal Shelf Sci.*, vol. 209, pp. 149–159, 2018, doi: 10.1016/j.ecss.2018.05.031.

[31] H. Mohebzadeh et al., "Spatial downscaling of MODIS chlorophyll-a with genetic programming in South Korea," *Remote Sens.*, vol. 12, 2020, Art. no. 1412, doi: 10.3390/rs12091412.

[32] H. Mohebzadeh and T. Lee, "Spatial downscaling of MODIS Chlorophyll-a with machine learning techniques over the west coast of the yellow sea in South Korea," *J. Oceanogr.*, vol. 77, pp. 103–122, 2021, doi: 10.1007/s10872-020-00562-6.

[33] J. H. Friedman, "Greedy function approximation: A gradient boosting machine," *Ann. Statist.*, vol. 29, pp. 1189–1232, 2001, doi: 10.1214/aos/1013203451.

[34] K. H. Mittenzwey et al., "Determination of chlorophyll a of inland waters on the basis of spectral reflectance," *Limnol. Oceanogr.*, vol. 37, no. 1, pp. 147–149, 1992, doi: 10.4319/lo.1992.37.1.0147.

[35] E. Svab et al., "Characterizing the spectral reflectance of algae in lake waters with high suspended sediment concentrations," *Int. J. Remote Sens.*, vol. 26, no. 5, pp. 919–928, 2005, doi: 10.1080/0143116042000274087.

[36] M. Beaulieu et al., "Nutrients and water temperature are significant predictors of cyanobacterial biomass in a 1147 lakes data set," *Limnol. Oceanogr.*, vol. 58, no. 5, pp. 1736–1746, 2013, doi: 10.4319/lo.2013.58.5.1736.

[37] J. U. Eitel et al., "Broadband, red-edge information from satellites improves early stress detection in a New Mexico conifer woodland," *Remote Sens. Environ.*, vol. 115, no. 12, pp. 3640–3646, 2011, doi: 10.1016/j.rse.2011.09.002.

[38] Z. Yigit Avdan et al., "Monitoring the water quality of small water bodies using high-resolution remote sensing data," *ISPRS Int. J. Geo-Inf.*, vol. 8, no. 12, 2019, Art. no. 553, doi: 10.3390/ijgi8120553.

[39] Y. T. Zhou et al., "Suitability of Sentinel-3 chlorophyll a products based on optical water types," *Int. J. Remote Sens.*, vol. 44, no. 4, pp. 1369–1389, 2023, doi: 10.1080/01431161.2023.2180780.

[40] J. Zhou et al., "Reconstruction of global MODIS NDVI time series: Performance of Harmonic Analysis of Time Series (HANTS)," *Remote Sens. Environ.*, vol. 163, pp. 217–228, 2015, doi: 10.1016/j.rse.2015.03.018.

[41] G. J. Roerink et al., "Reconstructing cloudfree NDVI composites using Fourier analysis of time series," *Int. J. Remote Sens.*, vol. 21, no. 9, pp. 1911–1917, 2000, doi: 10.1080/014311600209814.

[42] Y. Wang, F. Huang, and Y. Wei, "Water body extraction from LANDSAT ETM+ image using MNDWI and K-T transformation," in *Proc. 21st Int. Conf. Geoinform.*, 2013, pp. 1–5.

[43] R. Keys, "Cubic convolution interpolation for digital image processing," *IEEE Trans. Acoust., Speech, Signal Process.*, vol. 29, no. 6, pp. 1153–1160, Dec. 1981, doi: 10.1109/TASSP.1981.1163711.

[44] S. Mishra and D. R. Mishra, "Normalized difference chlorophyll index: A novel model for remote estimation of chlorophyll-a concentration in turbid productive waters," *Remote Sens. Environ.*, vol. 117, pp. 394–406, 2012, doi: 10.1016/j.rse.2011.10.016.

[45] P. A. Brivio et al., "Determination of chlorophyll concentration changes in Lake Garda using an image-based radiative transfer code for Landsat TM images," *Int. J. Remote Sens.*, vol. 22, no. 2/3, pp. 487–502, 2001, doi: 10.1080/014311601450059.

[46] S. Guo et al., "MODIS ocean color product downscaling via spatio-temporal fusion and regression: The case of chlorophyll-a in coastal waters," *Int. J. Appl. Earth Observ. Geoinf.*, vol. 73, pp. 340–361, 2018, doi: 10.1016/j.jag.2018.06.004.

[47] Y. Yang et al., "Improving lake chlorophyll-a interpreting accuracy by combing spectral and texture features of remote sensing," *Environ. Sci. Pollut. Res.*, vol. 30, pp. 83628–83642, 2023, doi: 10.21203/rs.3.rs-2571625/v1.

[48] R. Quiros, "Relationships between air temperature, depth, nutrients and chlorophyll in 103 Argentinian lakes," *Internationale Vereinigung Theoretische Und Angewandte Limnologie: Verhandlungen*, vol. 23, pp. 647–658, 1988, doi: 10.1080/03680770.1987.11899688.

[49] J. Ting, A. D'Souza, S. Vijayakumar, and S. Schaal, "Efficient learning and feature selection in high-dimensional regression," *Neural Comput.*, vol. 22, no. 4, pp. 831–886, Apr. 2010, doi: 10.1162/neco.2009.02-08-702.

[50] C. Hutengs and M. Vohland, "Downscaling land surface temperatures at regional scales with random forest regression," *Remote Sens. Environ.*, vol. 178, pp. 127–141, 2016, doi: 10.1016/j.rse.2016.03.006.

[51] P. Bartkowiak et al., "Downscaling land surface temperature from MODIS dataset with random forest approach over alpine vegetated areas," *Remote Sens.*, vol. 11, 2019, Art. no. 1319, doi: 10.3390/rs11111319.

[52] J. Xu et al., "Hybrid modelling of random forests and Kriging with Sentinel-2A multispectral imagery to determine urban brightness temperatures with high resolution," *Int. J. Remote Sens.*, vol. 42, pp. 2174–2202, 2020, doi: 10.1080/01431161.2020.1851801.

[53] G. Ke et al., "DeepGBM: A deep learning framework distilled by GBDT for online prediction tasks," in *Proc. 25th ACM SIGKDD Int. Conf. Knowl. Discov. Data Mining*, 2019, pp. 384–394.

[54] G. Xu et al., "Spatial downscaling of TRMM precipitation product using a combined multifractal and regression approach: Demonstration for South China," *Water*, vol. 7, no. 6, pp. 3083–3102, 2015, doi: 10.3390/w7063083.

[55] T. Hwang et al., "Downscaling real-time vegetation dynamics by fusing multi-temporal MODIS and Landsat NDVI in topographically complex terrain," *Remote Sens. Environ.*, vol. 115, no. 10, pp. 2499–2512, 2011, doi: 10.1016/j.rse.2011.05.010.

[56] R. Zebari et al., "A comprehensive review of dimensionality reduction techniques for feature selection and feature extraction," *J. Appl. Sci. Technol. Trends*, vol. 1, no. 2, pp. 56–70, 2020, doi: 10.38094/jastt1224.

[57] H. Yao et al., "Retrieval of chlorophyll-a concentrations in the coastal waters of the Beibu Gulf in Guangxi using a gradient-boosting decision tree model," *Appl. Sci.*, vol. 11, no. 17, 2021, Art. no. 7855, doi: 10.3390/app11177855.

[58] S. Xu et al., "Spatial downscaling of land surface temperature based on a multi-factor geographically weighted machine learning model," *Remote Sens.*, vol. 13, no. 6, 2021, Art. no. 1186, doi: 10.3390/rs13061186.

[59] L. Gao et al., "Localization or globalization? determination of the optimal regression window for disaggregation of land surface temperature," *IEEE Trans. Geosci. Remote Sens.*, vol. 55, no. 1, pp. 477–490, Jan. 2017, doi: 10.1109/tgrs.2016.2608987.
[60] Z. H. Yusuf, "Phytoplankton as bioindicators of water quality in Nasarawa reservoir, Katsina state Nigeria," *Acta Limnologica Brasiliensia*, vol. 32, 2020, Art. no. e4, doi: 10.1590/s2179-975x3319.
[61] C. E. Fergus et al., "Spatial variation in nutrient and water color effects on lake chlorophyll at macroscales," *PLoS One*, vol. 11, 2016, Art. no. e0164592, doi: 10.1371/journal.pone.0164592.
[62] X. Pi et al., "Chlorophyll-a concentrations in 82 large alpine lakes on the Tibetan Plateau during 2003–2017: Temporal–spatial variations and influencing factors," *Int. J. Digit. Earth*, vol. 14, pp. 714–735, 2021, doi: 10.1080/17538947.2021.1872722.
[63] G. Liu et al., "Remote sensing of CDOM and DOC in alpine lakes across the Qinghai-Tibet Plateau using Sentinel-2A imagery data," *J. Environ. Manage.*, vol. 286, 2021, Art. no. 112231, doi: 10.1016/j.jenvman.2021.112231.
[64] V. Markogianni et al., "An appraisal of the potential of Landsat 8 in estimating chlorophyll-a, ammonium concentrations and other water quality indicators," *Remote Sens.*, vol. 10, no. 7, 2018, Art. no. 1018, doi: 10.3390/rs10071018.
[65] B. A. Franz et al., "Ocean color measurements with the operational Land imager on Landsat-8: Implementation and evaluation in SeaDAS," *J. Appl. Remote Sens.*, vol. 9, no. 1, pp. 096070–096070, 2015, doi: 10.1117/1.JRS.9.096070.
[66] H. Duan et al., "Long-term temporal and spatial monitoring of Cladophora blooms in Qinghai Lake based on multi-source remote sensing images," *Remote Sens.*, vol. 14, no. 4, 2022, Art. no. 853, doi: 10.3390/rs14040853.
[67] M. Shen et al., "Sentinel-3 OLCI observations of water clarity in large lakes in eastern China: Implications for SDG 6.3.2 evaluation," *Remote Sens. Environ.*, vol. 247, 2020, Art. no. 111950, doi: 10.1016/j.rse.2020.111950.
[68] Y. Shang et al., "Factors affecting seasonal variation of microbial community structure in Hulun Lake, China," *Sci. Total Environ.*, vol. 805, 2022, Art. no. 150294, doi: 10.1016/j.scitotenv.2021.150294.
[69] Y. Liu et al., "Evaluation of trophic state for inland waters through combining Forel-Ule index and inherent optical properties," *Sci. Total Environ.*, vol. 820, 2022, Art. no. 153316, doi: 10.1016/j.scitotenv.2022.153316.
[70] S. Xu et al., "The fuzzy comprehensive evaluation (FCE) and the principal component analysis (PCA) model simulation and its applications in water quality assessment of Nansi Lake Basin, China," *Environ. Eng. Res.*, vol. 26, no. 2, 2021, Art. no. 200022, doi: 10.4491/eer.2020.022.

Simin Zhang received the Bachelor of Engineering degree in surveying and mapping engineering from the South China Agricultural University, Guangzhou, China, in 2021. She is currently working toward the master's degree in resources and environmental engineering with the School of Geography and Planning, Sun Yat-sen University, Guangzhou, China.

Her research interests include image processing, image downscaling, and bathymetry inversion.

Nanfeng Liu received the B.S. degree in remote sensing science and technology from the Nanjing University of Information Science and Technology, Nanjing, China, in 2009, the M.S. degree in cartography and GIS from the Institute of Remote Sensing Applications, Chinese Academy of Sciences, Beijing, China, in 2012, and the Ph.D. degree in geography from Queen's University, Kingston, Canada, in 2017.

He is currently an Associate Professor with Sun Yat-sen University, Guangzhou, China. His research interests include vegetation quantitative remote sensing, agricultural remote sensing, and hyperspectral remote sensing.

Ming Luo received the B.S. degree in remote sensing information engineering from the University of Wuhan, Wuhan, China, in 2007, the M.S. degree in geosciences and resources from the Chinese Academy of Sciences, Beijing, China, in 2010, and the Ph.D. degree in geography from the Chinese University of Hong Kong, Hong Kong, SAR, China, in 2014.

He is currently a Professor with Sun Yat-sen University, Guangzhou, China. His research interests include global change and extreme weather and climate, urban climate and habitat, environmental health, and spatial and temporal big data analysis.

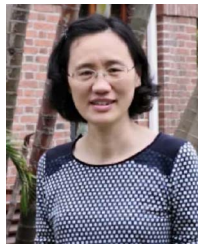

Tao Jiang received the B.S. and M.S. degrees in geography from Sun Yat-sen University, Guangzhou, China, in 1989 and 1992, respectively, and the Ph.D. degree in geography from the Chinese University of Hong Kong, Hong Kong, SAR, China, in 2005.

She is currently an Associate Professor with Sun Yat-sen University. Her research interests include water environment planning and assessment, water environmental protection, and environmental hydraulics.

Ting On Chan received the B. Eng. degree in electronic engineering (information & communication engineering), from the Hong Kong University of Science and Technology, Hong Kong, SAR, China, in 2003, the M.Sc. degree in applied environmental measurement techniques from the Chalmers University of Technology, Gothenburg, Sweden, in 2005, and the M.Sc. and Ph.D. degrees in geomatics engineering from the University of Calgary, Calgary, AB, Canada, in 2012 and 2015, respectively.

He is currently an Associate Professor with Sun Yat-sen University, Guangzhou, China. His research interests include LiDAR and photogrammetry applications, environmental monitoring, and oceanic and climatological analyses.

Cynthia Sin Ting Yau received the Ph.D. degree in zoology from the University of Aberdeen, Aberdeen, U.K., in 1994.

She is currently a Lecturer with the Hong Kong University of Science and Technology, Hong Kong, SAR, China. Her research interests include biodiversity, marine ecology, marine environment, marine plankton ecology, and marine conservation.

Yeran Sun received the B.S. degree in GIS from Northwest University, Xi'an, China, in 2008, the M.S. degree in cartography and GIS from the University of Chinese Academy of Sciences, Beijing, China, in 2011, and the Ph.D. degree in geographic information science from Heidelberg University, Heidelberg, Germany, in 2015.

He is currently a Senior Lecturer with the University of Lincoln, Lincoln, U.K. His research interests include quantitative human geography, GIS, healthy built environment, and geospatial big data analytics.